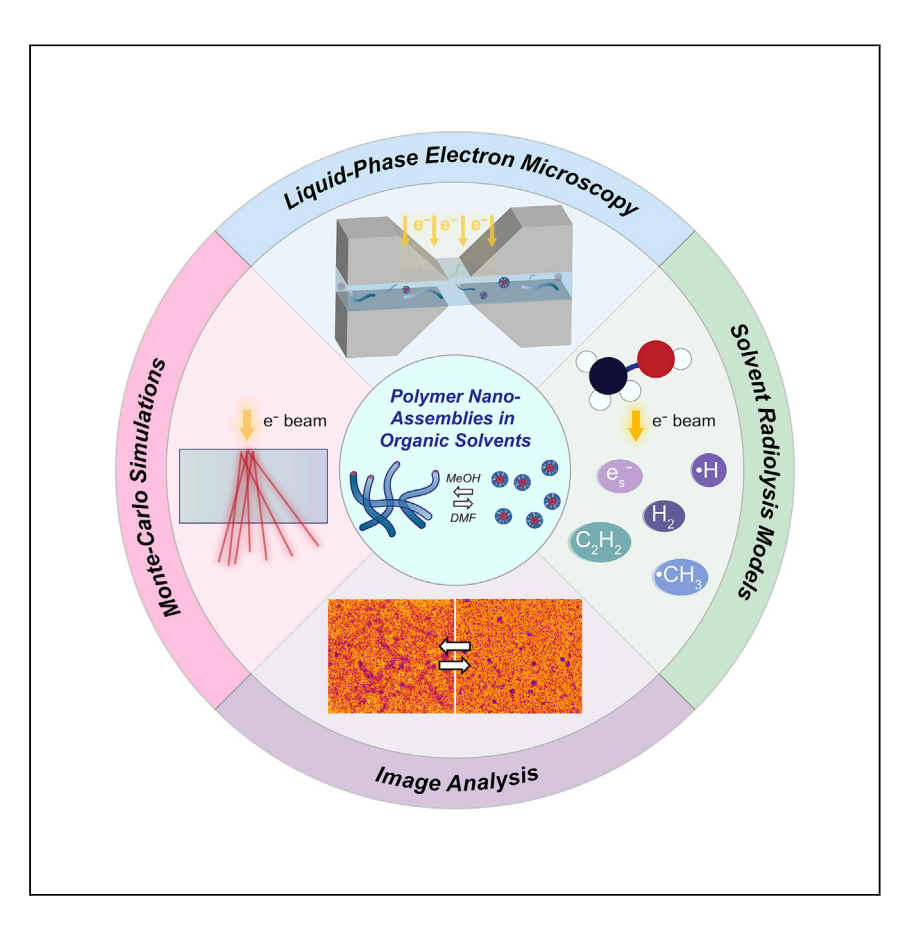


#### **Article**

# Organic solution-phase transmission electron microscopy of copolymer nanoassembly morphology and dynamics



Direct imaging of nanomaterials in organic solvents is an unmet need in chemistry and materials science. Korpanty et al. report a multimodal strategy to study dynamic, polymeric nanomaterials in organic solvents, leveraging Monte Carlo simulations, radiolysis models, and image processing to enable the observation of solvated nanomaterials via liquid-phase transmission electron microscopy.

Joanna Korpanty, Karthikeyan Gnanasekaran, Cadapakam Venkatramani, Nanzhi Zang, Nathan C. Gianneschi

nzang@gene.com (N.Z.) nathan.gianneschi@northwestern.edu (N.C.G.)

#### Highlights

Imaged PS-b-P4VP nanoassemblies in DMF, MeOH, and  $H_2O$  via LCTEM correlated by MALDI-IMS

Models and experiments showed H<sub>2</sub>O is more radiolytically sensitive than DMF and MeOH

Observed the worm-to-micelle phase transition for PS-*b*-P4VP via solvent exchange

Nanomaterials dispersed in organic solvents should be a focus of future LCTEM studies

Korpanty et al., Cell Reports Physical Science 3, 100772

March 16, 2022 © 2022 The Author(s). https://doi.org/10.1016/j.xcrp.2022.100772





#### **Article**

# Organic solution-phase transmission electron microscopy of copolymer nanoassembly morphology and dynamics

Joanna Korpanty,<sup>1</sup> Karthikeyan Gnanasekaran,<sup>1</sup> Cadapakam Venkatramani,<sup>2</sup> Nanzhi Zang,<sup>2,\*</sup> and Nathan C. Gianneschi<sup>1,3,4,\*</sup>

#### **SUMMARY**

Direct imaging of the dynamics of polymeric assemblies in organic solvents is an outstanding challenge. Herein, we apply liquid cell transmission electron microscopy (LCTEM) to study polymeric nanomaterials in organic solvents. LCTEM is distinct from other TEM methods as it can be applied to characterize the morphology of nanomaterials in organic solvents. To enable this demonstration, we examined electron-solvent interactions for two common organic solvents, N,N-dimethylformamide and methanol, and compared these solvents to water. For each solvent, we developed Monte Carlo simulations and kinetic radiolysis models, providing scattering and chemical insight, respectively. Guided by theoretical results, we applied LCTEM and postmortem mass spectral imaging of poly(styrene)-b-poly(4-vinylpyridine) assemblies in each solvent. Then, a worm-to-micelle transformation in poly(styrene)-b-poly(4-vinylpyridine) was triggered via organic solvent mixing during LCTEM, enabling an experiment not possible through a cryogenic TEM time series. Our work provides a pathway for an expanded examination of nanomaterials in organic solvents via LCTEM, a neglected research area despite the obvious prevalence of such materials across chemistry and materials science.

#### INTRODUCTION

Amphiphilic polymeric assemblies have attracted broad interest for their ability to form solution-phase hierarchical assemblies, including micelles, wormlike micelles, vesicles, bicontinuous structures, and toroids. Their tunable assembly behavior has motivated researchers to employ polymeric nanomaterials in catalysis, <sup>2,3</sup> templating, 4,5 and nanomaterial fabrication. 6,7 Although numerous methods synthesize, prepare, and employ polymeric amphiphiles and their assemblies in organic solvents, <sup>6,8,9</sup> standardized methods that provide direct, nanoscale insight into the solvated morphologies of these polymeric systems are lacking. Specifically, electron microscopy techniques, such as dry-state transmission electron microscopy (TEM), often require sample drying, resulting in image artifacts that may not reflect the true solution-phase morphology. 10 Furthermore, while cryogenic (cryo) TEM can enable vitrification of solvated morphologies, it is only reliable and robust for aqueous samples, as it has mostly been a methodology tailored to structural biology. 11-13 Standard methods used in sample preparation for aqueous phase cryo-TEM are inherently difficult to adapt to organic solvents, with very little work done in this area. 14-16



<sup>&</sup>lt;sup>1</sup>Department of Chemistry, International Institute for Nanotechnology, Chemistry of Life Processes Institute, Simpson Querrey Institute, Northwestern University, Evanston, IL 60208, USA

<sup>&</sup>lt;sup>2</sup>Small Molecule Analytical Chemistry, Genentech, South San Francisco, CA 94080, USA

<sup>&</sup>lt;sup>3</sup>Department of Materials Science & Engineering, Department of Biomedical Engineering and Department of Pharmacology, Northwestern University, Evanston, IL 60208, USA

<sup>&</sup>lt;sup>4</sup>Lead contact

<sup>\*</sup>Correspondence: nzang@gene.com (N.Z.), nathan.gianneschi@northwestern.edu (N.C.G.) https://doi.org/10.1016/j.xcrp.2022.100772



Given the challenges that face standard TEM and cryo-TEM for organic solvated systems, direct imaging of nanoscale organic materials in organic solvents is an unmet need in chemistry and materials science. Therefore, we turn here to the development of liquid cell transmission electron microscopy (LCTEM). By hermetically sealing a liquid sample between two silicon microchips, LCTEM enables the direct visualization of solvated nanomaterials in real time. 17-19 Despite its potential utility for imaging polymeric nanomaterials dispersed in organic solvents, LCTEM has never been used to simply image the solution-phase morphology of such a system. Rather, the majority of LCTEM studies on polymeric materials have been performed under aqueous conditions, 20-22 with several recent experiments having been performed in aqueous solution with organic solvents as additives.<sup>23,24</sup> The lack of LCTEM studies performed in organic solvents is partially due to a lack of understanding about how the electron beam interacts with different solvents and because of a steady focus on aqueous phase systems within the field. Given the potential for reactive species generated from beam-induced solvent radiolysis to perturb sample chemistry regardless of solvent, <sup>25–30</sup> it is critical to first understand organic solvent radiolysis in the context of LCTEM, but such studies have only been conducted for aqueous solutions. 24,25,30

Aiming to build fundamental insight into electron-solvent interactions, we describe the coupling of experiment, simulations, and modeling to elucidate electron-solvent interactions for two organic solvents, *N*,*N*-dimethylformamide (DMF) and methanol, which were chosen due to their increasing use in LCTEM studies. <sup>18,31,32</sup> We use GEANT4 Monte Carlo simulations, which assess electron-sample interactions from a scattering perspective, combined with COMSOL radiolysis modeling, which provides chemical insight into electron-sample interactions. Modeled and simulated results for the organic solvents were then compared to water. We experimentally verified the models for a test system, poly(styrene)-*b*-poly(4-vinylpyridine) dispersed in DMF, methanol, or water. The system was studied via LCTEM, and the chemical structure of the polymer, following imaging with the electron beam, was then verified via matrix-assisted laser desorption/ionization imaging mass spectrometry (MALDI-IMS) of the imaged area. <sup>24,33</sup>

#### **RESULTS AND DISCUSSION**

#### **Monte Carlo simulations**

To develop a GEANT4 simulation representative of LCTEM conditions, a literature precedent employing GEANT4 to model a scanning transmission electron microscope (STEM) was amended. <sup>34</sup> In brief, the amended Monte Carlo simulation incorporates an electron source operated at 300 keV, as is typical for an LCTEM microscope, <sup>18,24,33,35,36</sup> and the underlying physics accounts for multiple scattering under the penetration and energy loss of positions and electrons (Penelope) system. <sup>37</sup> The three-dimensional sample geometry mirrors the typical liquid cell window size of  $50 \times 50 \, \mu m$  in the x and y dimensions (Figure 1). Given the variability of the liquid thickness across liquid cell experiments, we simulated liquid cells with liquid layers between 100 nm and 10  $\mu m$  containing DMF, methanol, or water (Figure 1A). Each simulation was repeated three times with one million primary electrons. To assess electron-solvent interactions for each solvent, the average number of secondary electrons (SEs), the average absorbed energy, and the average absorbed dose were measured by a detector placed in the center of the sample geometry (Figures 1B–1D and S1–S3).

Across the examined liquid thicknesses, the average number of SEs is close for water and methanol, while DMF slightly surpasses these solvents at higher

#### **Article**



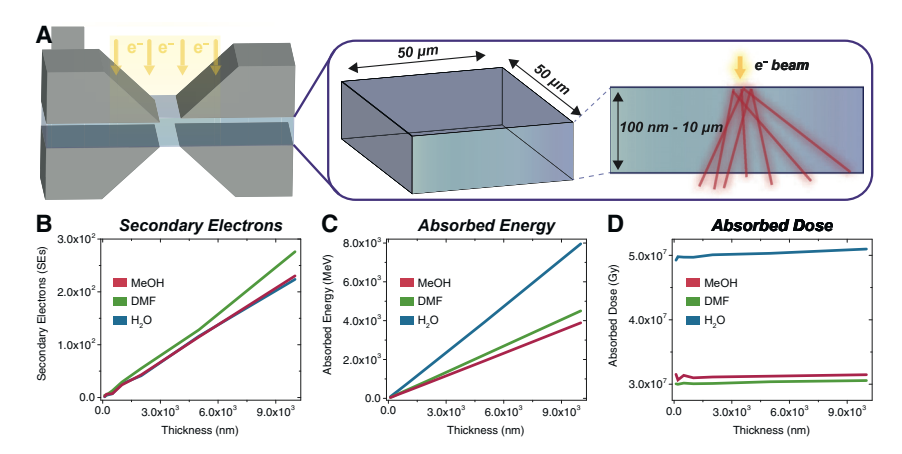


Figure 1. GEANT4 Monte Carlo simulation setup and results

(A) Liquid-cell assembly with the inset showing the geometric setup of a simulated liquid cell. (B–D) (B) Average secondary electron generation, (C) absorbed energy, and (D) absorbed dose for methanol, N,N-dimethylacrylamide, and water over liquid layers in the range of 100 nm to 10 µm.

thicknesses (Figure 1B). The increased SE generation in DMF may be due to the comparatively high molar concentration of DMF (77.4 mol L $^{-1}$ ) relative to methanol (40.5 mol L $^{-1}$ ) and water (55.5 mol L $^{-1}$ ), the pure solutions of which these systems approximate. Given the increased SE generation in DMF, the simulated results indicate that the contribution of SEs to solvent damage should be highest for DMF, whereas water and methanol should be similarly affected. For all three solvents, the average number of SEs generated increases with increasing thickness and, at lower thicknesses, the difference in SE generation for the three solvents is minimized. However, given the similarity in SE generation for all three solvents at the low liquid thicknesses most relevant for LCTEM (<1  $\mu$ m), the simulated results suggest that SE generation contributes similarly to electron beam-induced damage in all three solvents.  $^{38}$ 

On the other hand, the absorbed energy is highest for water, followed by DMF, and finally methanol (Figure 1C). Since water has the highest density, electrons penetrating through the sample lose more energy compared to less dense solvents. Likewise, for thicker samples, more energy is lost when electrons travel through the sample, manifesting in an increase in the absorbed energy (Figure 1C). Similarly, the absorbed dose is highest for water, followed by methanol, and then DMF (Figure 1D). The absorbed dose results can be rationalized by considering the elemental composition of each solvent, particularly the percentage of oxygen, the heaviest constituent element. Water is roughly composed of 88% oxygen, compared to 50% for methanol, and 22% for DMF. Since the absorbed dose measures the energy absorbed per unit mass, the results correlate with the percentage of oxygen, thus resulting in water having the highest absorbed dose and DMF the lowest. As with the absorbed energy and number of SEs, the absorbed dose increases with liquid thickness when each solvent is examined individually (Figures \$1–\$3).

Taken together, the Monte Carlo simulation results suggest that water should undergo the most damaging electron-solvent interactions. For all three solvents, the number of generated SEs does not vary greatly, specifically at the low liquid thicknesses typical for LCTEM (100 nm to 1  $\mu$ m).<sup>39</sup> However, for all liquid thicknesses, both the absorbed dose and energy are far higher for water compared to the two organic solvents. Ultimately, these results indicate that, from a scattering



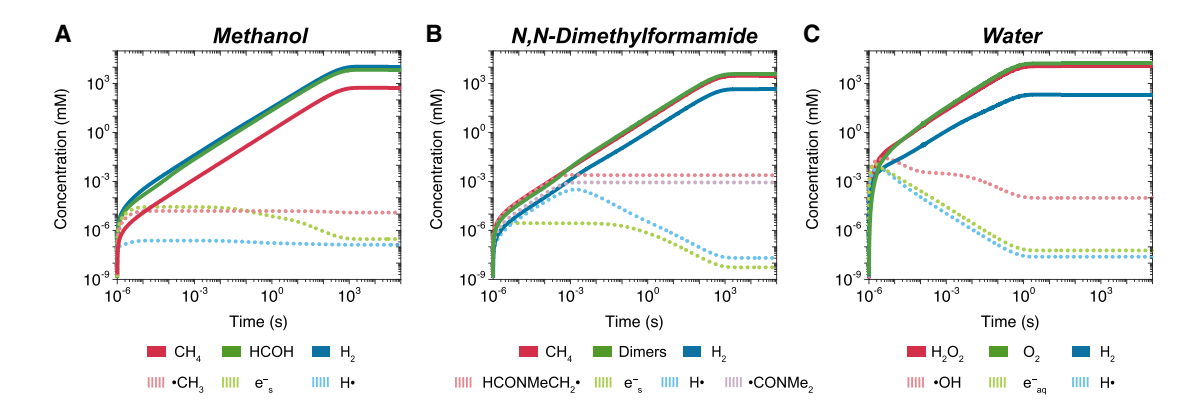


Figure 2. Modeled results for solvent radiolysis using the reaction engineering module in COMSOL (A–C) Results for (A) methanol, (B) N,N-dimethylformamide, and (C) water. Note that dimers formed in DMF result from self or mixed reactions between HCONMeCH<sub>2</sub>• and •CONMe<sub>2</sub> radicals. For all three simulations, a 300 keV electron beam with a beam current of 1 nA and radius of 1 μm were

perspective, aqueous solutions are likely more prone to electron beam-induced damage. Correlated with this increased electron beam-induced solvent damage, the more strongly scattered electrons would be expected to lead to lower image contrast compared to organic solvents when attempting to image low contrast solvated organic materials, pointing to the value in expanding LCTEM to the study of organic nanomaterials in organic solvents.

#### **Radiolysis modeling**

Seeking more chemical insight into solvent damage, we next endeavored to model radiolysis for methanol, DMF, and water (Figure 2). Using the reaction engineering module in the multiphysics software COMSOL, we developed a kinetic model for the radiolysis of each solvent under LCTEM conditions. Mirroring previous studies, <sup>24,25</sup> we assume all radiolytic species are homogeneously distributed in the irradiated solvent and that the concentration of each solvent remains constant. The concentration for each radiolytic species was calculated by summing the rates of individual reactions between different radiolytic species and the yield due to direct irradiation. Under a fixed beam current and diameter, we note that the delivered dose, measured in Gy s<sup>-1</sup>, varies slightly for each solvent, as each solvent has a unique density-normalized stopping power. <sup>25,40</sup> In all cases, numerous radiolytic species are generated, and we consider a subset of the radical and molecular species formed in methanol, DMF, and water (Figures 2A–2C; Tables S1–S6).

For our modeled results, there are several clear distinctions between the three solvents. The radiolytic species generated from methanol and DMF reach a steady-state concentration the slowest, taking roughly 1,000 s, compared to 1 s for water. In contrast to DMF and water, the radical species generated from methanol, namely the methyl radical ( ${}^{\bullet}\text{CH}_3$ ), solvated electron ( ${}^{e}\text{S}_3$ ), and hydrogen atom ( ${}^{\bullet}\text{H}_3$ ), all remain below  ${}^{\sim}10^{-4}$  mM for the entire simulation ( ${}^{10^{-6}-10^3}$  s).

Since all three solvents form  $H^{\bullet}$  and  $e_s^-$ , we examine the reactivity of the radicals unique to each solvent, namely  ${}^{\bullet}\text{CH}_3$  in methanol, HCONMeCH $_2^{\bullet}$  and  ${}^{\bullet}\text{CONMe}_2$  in DMF, and  ${}^{\bullet}\text{OH}$  in water. It is well established that radicals centered on more electronegative atoms are less stable, resulting in a high reactivity for  ${}^{\bullet}\text{OH}$  radicals generated in water compared to the carbon-centered radicals formed in the two organic solvents.  ${}^{41,42}$  The two radicals generated from DMF, although distinct in stability, are both less reactive than the comparatively unstable  ${}^{\bullet}\text{CH}_3$  radicals



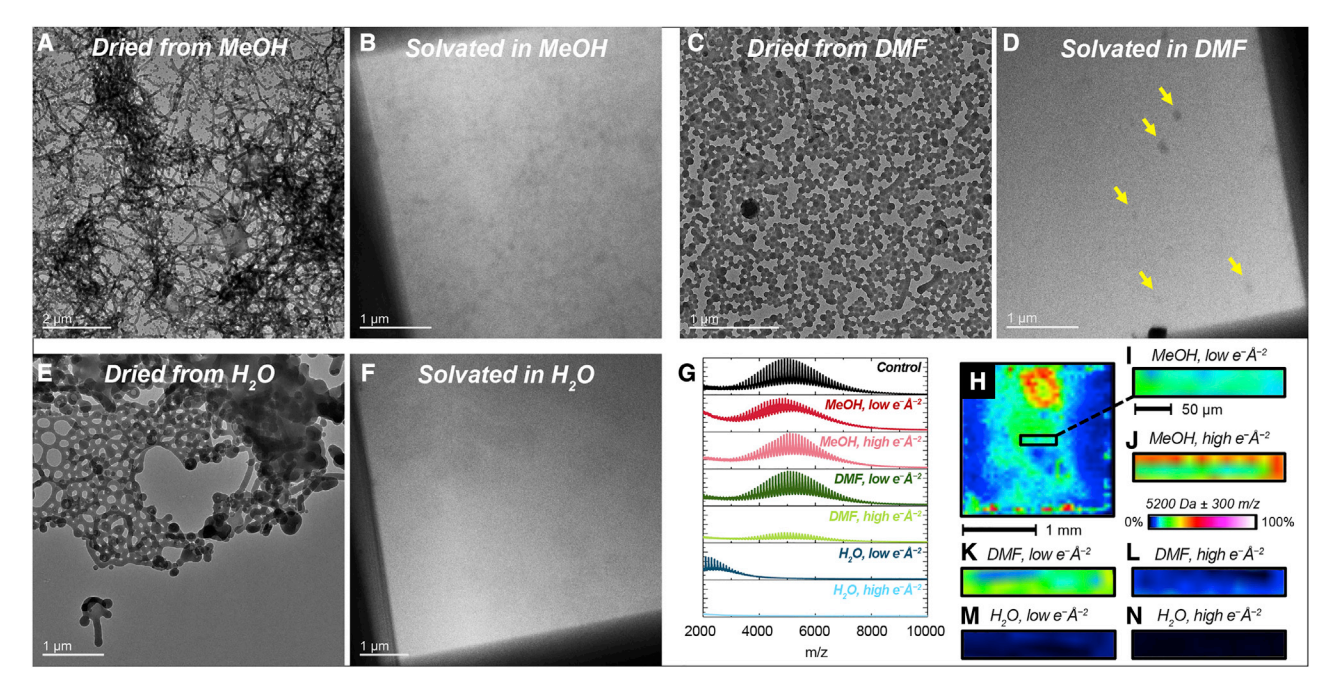


Figure 3. Imaging and mass spectral results for PS-b-P4VP assemblies dispersed in different solvents

(A–D) PS-b-P4VP assemblies in methanol imaged via (A) dry state and (B) LCTEM. PS-b-P4VP assemblies in DMF imaged via (C) dry state and (D) LCTEM. (E and F) PS-b-P4VP assemblies in methanol imaged via (E) dry state and (F) LCTEM.

(G–N) (G) MALDI mass spectra from top to bottom for unimaged control, methanol imaged at low flux (0.8 e  $^{-}$ Å  $^{-2}$ s  $^{-1}$ , 4.0 e  $^{-}$ Å  $^{-2}$ ), methanol at high flux (14.7 e  $^{-}$ Å  $^{-2}$ s  $^{-1}$ , 8.82  $\times$  10 $^{3}$  e  $^{-}$ Å  $^{-2}$ ), DMF at low flux, DMF at high flux, water at low flux, and water at high flux. MALDI-IMS mass-filtered color maps for (H) small chip and (I) window for methanol imaged at low flux, (J) window for methanol imaged at high flux, (K) window for DMF imaged at low flux, (L) window for DMF imaged at high flux. MALDI-IMS color maps are shown with a mass filter of 5,200  $\pm$  300 m/z displayed as 0%–100% of total intensity on a logarithmic scale.

generated from methanol.<sup>43,44</sup> We note that there is no evidence in the radiation chemistry literature that \*OH radicals are generated in methanol, likely due to the scavenging of \*OH radicals by methanol.<sup>45</sup>

In brief, based purely on radical reactivity,  $^{\bullet}$ OH radicals generated from water are likely to cause the most secondary damage to the sample under study, and previous studies have demonstrated the destructive nature of these radicals to soft matter in particular.  $^{24,46-49}$  It is worth noting that the HCONMeCH2 $^{\bullet}$  and  $^{\bullet}$ CONMe2 radicals generated in DMF, although the least reactive, attain the highest steady-state concentrations ( $^{\sim}10^{-3}$  mM) compared to  $^{\bullet}$ CH3 ( $^{\sim}10^{-5}$  mM) and  $^{\bullet}$ OH ( $^{\sim}10^{-4}$  mM) radicals formed in methanol and water, respectively; this suggests that DMF likely shows intermediate radiolytic sensitivity. Finally,  $^{\bullet}$ CH3 radicals generated in methanol are not only less reactive than  $^{\bullet}$ OH radicals generated in water, but also attain the lowest steady-state concentration of the examined radicals, suggesting that methanol is more amenable to LCTEM than water.

#### **LCTEM and MALDI-IMS**

With modeled results in hand, we next aimed to image poly(styrene)-b-poly(4-vinylpyridine) (PS-b-P4VP) polymeric assemblies dispersed in the organic solvents. This class of polymer was chosen due to the numerous previous studies focused on the phase behavior of the polymer in organic solvents. <sup>50–52</sup> For our studies, we specifically utilized PS<sub>116</sub>-b-P4VP<sub>23</sub> assemblies prepared in methanol, DMF, or water (Figure 3). To characterize the nanoscale structures, we utilized both dry-state TEM, dynamic light scattering (DLS) (Figure S6), and LCTEM. For the sample prepared in methanol, the assemblies



appeared to be large, tangled worms by dry-state TEM with clear drying and aggregation artifacts (Figure 3A). Overcoming the artifacts of dry-state TEM, LCTEM clearly showed the presence of worms in methanol at a flux of  $0.8 \, \mathrm{e^{-\,\mathring{A}^{-2}\,s^{-1}}}$ , enabling the first of its kind observation of a polymeric nanoassembly in liquid methanol (Figure 3B). Next, we visualized assemblies dispersed in DMF via dry-state TEM and LCTEM. As observed via dry-state TEM imaging, the assemblies appeared to be aggregated micellar nanoparticles. In LCTEM, micelles were likewise observed at a flux of 0.8 e<sup>-</sup>  $\mathring{A}^{-2}$  s<sup>-1</sup> (Figures 3C and 3D). Finally, we imaged assemblies dispersed in water. By dry-state TEM, the assemblies appeared to have undergone drying and aggregation effects, making the morphology unclear (Figure 3E). Similarly, in liquid, the high density of water prevented any meaningful morphological insight at the same flux of  $0.8 \, e^{-} \, \mathring{A}^{-2}$ s<sup>-1</sup> employed for the other two experiments (Figure 3F). In agreement with modeled results, LCTEM data further affirm the value in exploring methanol or related solvents in LCTEM over aqueous systems. We note that, for LCTEM experiments, it is difficult to control the liquid thickness via sample dropcasting and so the effect of varying liquid thickness could not be easily explored. For all experiments, however, imaging was conducted at minimal liquid thickness (<1 µm).

To evaluate sample survival following LCTEM imaging, we utilized a lower molecular weight  $PS_{33}$ -b- $P4VP_{31}$  polymer that could be ionized more efficiently by MALDI-IMS than the larger  $PS_{116}$ -b- $P4VP_{23}$  polymer. We have previously demonstrated the ability of MALDI-IMS to serve as a postmortem technique for imaged liquid cell chips to evaluate sample survival after imaging with high spatial resolution.  $^{24,33}$  We conducted two liquid cell experiments on the lower molecular weight  $PS_{33}$ -b- $P4VP_{31}$  polymer dispersed in each solvent: a stroboscopic imaging experiment in which each sample was imaged once every 3 min at  $0.8 e^- \ \mathring{A}^{-2} \ s^{-1}$  with a cumulative fluence of  $4.0 e^- \ \mathring{A}^{-2}$  and a continuous imaging experiment at  $14.7 e^- \ \mathring{A}^{-2} \ s^{-1}$  with a cumulative fluence of  $8.82 \times 10^3 \ e^- \ \mathring{A}^{-2}$  (Figures 3G–3N; Figure S4; Videos S1, S2, and S3).

Under stroboscopic imaging conditions, the overall mass spectra of the imaged windows show that PS-b-P4VP has similar mass signal retention when imaged in methanol and DMF (Figure 3G). However, under stroboscopic imaging in water, the PS block appears to be selectively degraded, and the remaining lower-molecular-weight signal has a spacing that corresponds to the 4-vinylpyridine monomer mass (Figure S5). However, under higher flux and fluence conditions, the PS-b-P4VP polymer signal is retained in methanol, reduced in DMF, and obliterated in water. We note that, in agreement with previous studies, a reduction in polymer mass signal intensity could indicate sample scission, leading to a low molecular weight signal or crosslinking. <sup>24,53</sup> The MALDI-IMS results agree with modeled and simulated results, both of which indicate that water should undergo the most solvent damage of the three solvents examined. The LCTEM and MALDI-IMS data reaffirm the value in studying non-aqueous nanomaterials via LCTEM, particularly in methanol or related alcoholic solvents. Not only are such alcoholic solvents less dense, enabling higher contrast, but they form less-reactive radicals at lower concentrations compared to water (Figures 2A and 2C).

Finally, having confirmed the radiation sensitivity of water through both experimentation and modeling, we endeavored to visualize the polymeric nanoassembly dynamics of PS-b-P4VP in purely organic solvents. Specifically, we aimed to trigger a worm-to-micelle transformation *in situ* by mixing worms in methanol with DMF (Figure 4; Figure S6). To ensure sample survival, specifically in the seemingly more sensitive DMF solvent, we employed a flux of  $0.8 \, \mathrm{e}^{-} \, \mathrm{Å}^{-2} \, \mathrm{s}^{-1}$  and a cumulative fluence of  $4.0 \, \mathrm{e}^{-} \, \mathrm{Å}^{-2}$ , reproducing the conditions under which the polymer was shown to survive in both DMF and methanol (Figures 3G and 4A).



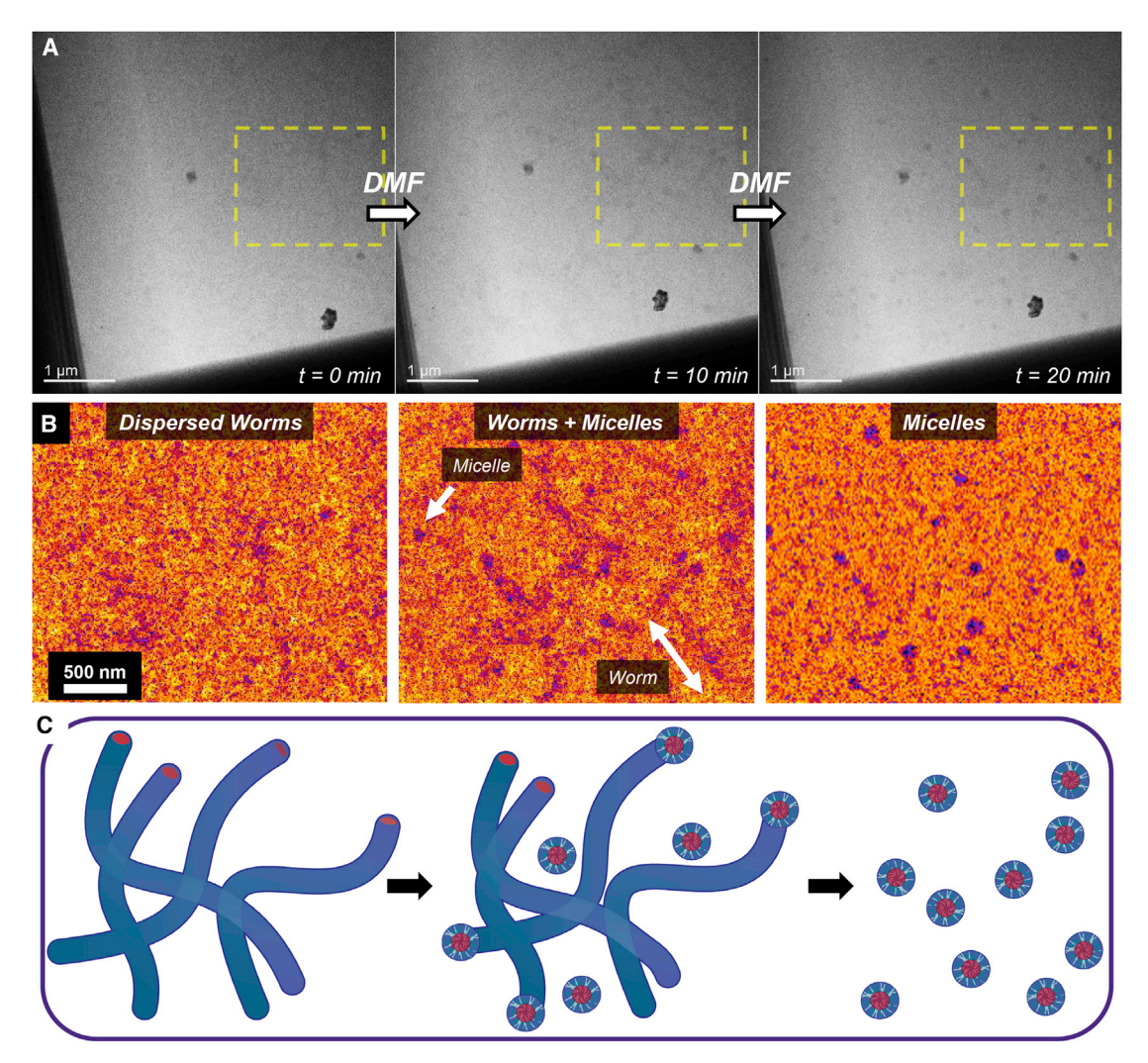


Figure 4. LCTEM results for PS-b-P4VP assemblies undergoing solvent switch from methanol to DMF imaged at 0.8 e<sup>-</sup> Å<sup>-2</sup> s<sup>-1</sup>
(A) Three LCTEM images during *in situ* solvent switch with yellow dotted squares highlighting regions of interest for image processing.
(B) Image processing for region of interest performed by cropping, subtracting background, applying 4 × 4 average binning, and implementing a "fire"

 $\hbox{(C) Proposed mechanism for worm-to-micelle transformation during solvent switch.} \\$ 

Initially, in pure methanol, we observed diffuse worms throughout the liquid cell, as observed in repeat experiments (Figures S7–S8). Upon flowing DMF into the liquid cell with the electron beam blanked, we observed the formation of dense micellar structures. To aid in image interpretation, we performed image processing on a selected region of interest using ImageJ (Figure 4B). Specifically, we performed a background subtraction, 4 × 4 average binning, and applied a color filter by which each gray scale pixel was assigned a corresponding RGB value; using a color filter allowed us to better differentiate between dense micelles and more diffuse worms (Figure 4B). After a further 10 min of flowing in DMF with the beam off, the worms appeared to have fully transformed into micelles, and subsequent time points showed no further morphological evolution (Figure S8).

LCTEM data of the solvent-induced transformation suggest that the worms transition to micellar particles gradually, with micelles seemingly forming from and around



diffuse worms (Figure 4C). As worms do not fully redissolve to reform micelles, our LCTEM results suggest that the PS and P4VP blocks do not undergo core-corona inversion upon solvent switching. <sup>51</sup> Thus, since methanol preferentially solubilizes the P4VP block, our results imply that, in both DMF and methanol, the core is composed of PS and the corona of P4VP, in agreement with existing studies. <sup>54,55</sup> As the worm-to-micelle transformation was induced by the mixing of two organic solvents, such an insight likely could not be obtained by a cryo-TEM time series, as such a study would require optimization of vitrification conditions for DMF, methanol, and different compositions of the two solvents.

In summary, utilizing a multimodal approach with newly developed Monte Carlo simulations and radiolysis models, we have gained critical insight into electron-solvent interactions for DMF, methanol, and water, which will enable the study of soft nanomaterials dispersed in organic solvents via LCTEM. Both Monte Carlo simulations of electron trajectories through the solvents and kinetic modeling of radiolysis indicate that water is the most radiolytically sensitive of the three solvents, while the organic solvents appear comparatively stable. Our modeled findings were verified via LCTEM and MALDI-IMS experiments performed on poly(styrene)-bpoly(4-vinylpyridine) dispersed in either DMF, methanol, or water. Using optimized imaging conditions and guided by modeled results, we visualized a worm-to-micelle transformation in poly(styrene)-b-poly(4-vinylpyridine) assemblies, which was triggered by a methanol-to-DMF solvent switch. The solvent mixing experiment, not possible by standard techniques, such as cryo-TEM, provides direct mechanistic insight into the phase dynamics of poly(styrene)-b-poly(4-vinylpyridine) nanoassemblies. Thus, we conclude that radiation-sensitive soft nanomaterials dispersed in organic solvents should be more routinely studied with LCTEM. Such studies concerning morphology and dynamics can be used to directly probe specific polymeric systems, with correlation to scattering experiments and where standard imaging methods cannot easily be employed.<sup>53</sup>

#### **EXPERIMENTAL PROCEDURES**

#### Resource availability

#### Lead contact

Further information and requests for resources and reagents should be directed to and will be fulfilled by the lead contact, Nathan Gianneschi (nathan.gianneschi@northwestern.edu).

#### Materials availability

This study did not generate new unique reagents.

#### Data and code availability

All other data and code supporting the findings of this study are available within the article and are described in the supplemental information or are available from the corresponding author upon reasonable request.

#### Materials

 $PS_{116}$ -b- $P4VP_{23}$  and  $PS_{33}$ -b- $P4VP_{31}$  were purchased from Polymer Source and used as received. All other materials were purchased from Sigma and used as received unless otherwise noted.

#### Sample preparation

PS-b-P4VP (PS<sub>116</sub>-b-P4VP<sub>23</sub> or PS<sub>33</sub>-b-P4VP<sub>31</sub>) powder was dissolved in a vial with tetrahydrofuran (THF) at a concentration of 0.125 mg  $\mu$ L<sup>-1</sup>. The solution was stirred

#### Article



overnight, and the THF was removed with a stream of nitrogen. Then, methanol, DMF, or milli-Q water (pH 5) was added to the dried polymer sample to again achieve a concentration of 0.125 mg  $\mu L^{-1}$ . The solution was stirred for 3 days to yield an opaque solution of nanoassemblies.

#### **LCTEM** imaging

The Protochips Poseidon Select Heating holder was used to collect LCTEM data. The lines of the holder were prefilled with either methanol, DMF, or water in all LCTEM experiments. LCTEM chips with 50-nm-thick, 200  $\times$  50  $\mu m$  window  $SiN_x$  membranes were cleaned in acetone followed by methanol, dried, and subsequently glow discharged in a PELCO easiGlow glow discharge unit for 5 min. Next, 0.5  $\mu L$  of sample was pipetted manually onto the bottom chip, and then the liquid cell was assembled with the windows (50  $\times$  200  $\mu m$ ) aligned perpendicularly (50  $\times$  50  $\mu m$  LCTEM viewing area), and the lines of the holder were sealed off without external flow. For the data shown in Figure 4, the lines were prefilled with DMF, and the sample dropcasted on the chips was dispersed in methanol. Then, using a syringe pump at a rate of 1  $\mu L$  min $^{-1}$ , DMF was flowed into the viewing window of the LCTEM holder.

Experiments were performed using a JEM-ARM300F (JEOL, Tokyo, Japan) operated at 300 keV. Micrographs were recorded on a 2k × 2k Gatan OneView-IS CCD camera (Gatan, Pleasanton, CA, USA) using Gatan Digital Micrograph image acquisition software (Roper Technologies, Sarasota, FL, USA). The electron flux values used in LCTEM experiments were calculated using the beam current for each aperture selection, as measured by a Faraday Holder through vacuum, and the beam diameter incident upon the sample. For video acquisition, Camtasia Studio 2018 was used to record the screen at 30 frames per second (TechSmith, USA).

#### **MALDI-IMS**

LCTEM chips, with their  $SiN_x$  membranes facing upward, were adhered to the conductive face of an ITO-coated glass slide with 70–100  $\Omega$  resistivity (Bruker Daltonics), using  $\sim$ 0.5  $\mu$ L nail polish and allowed to dry. To equalize the height difference from  $SiN_x$  chips on the slide ( $\sim$ 0.25 mm), four pieces of Scotch tape were applied to both short edges of the slide on the same side. As a control, unimaged PS<sub>33</sub>-b-P4VP<sub>31</sub> at 0.125 mg  $\mu$ L<sup>-1</sup> in THF was dropcasted onto a clean liquid cell chip. All chips were coated with *trans*-2-[3-(4-*tert*-butylphenyl)-2-methyl-2-propenylidene] malononitrile matrix in (20 mg mL<sup>-1</sup> in THF).

Slides were mounted into an MTP Slide Adapter II and loaded onto a Bruker Rapiflex MALDI-ToF mass spectrometer for analysis using the flexControl software (Bruker Daltonics). Samples were analyzed by MALDI-MS under reflector positive mode (2,000–10,000 Da) using a 355 nm smartbeam 3D laser with a 50  $\mu$ m focus diameter and 200 Hz frequency, a constant laser power of 50%, and a sum of 500 shots per spectrum. Spectra were collected using an accelerating voltage of 20 kV and detector gain of 792 V. Region of interest mapping was performed at a raster width of 50  $\mu$ m, and image analysis was performed in flexImaging software (Bruker Daltonics).

For each MALDI-IMS experiment performed for chips imaged in the liquid cell, the mass spectra displayed in the main text (Figure 4G) were generated by averaging the mass spectra of the windows for the two chips used in the liquid cell assembly; that is, the spectra generated from the top chip and the bottom chip, which together comprise the liquid cell, are averaged. For the mass signal of PS<sub>33</sub>-b-P4VP<sub>31</sub> from irradiated chips to be visible compared to an unimaged control, the overall intensity of the mass spectrum was set to 50% of the total intensity of the control mass spectrum.



#### DLS

DLS measurements were performed on a Zetasizer (Malvern Instruments, Nano ZS) with a 60 s equilibrium time for each measurement.

#### **Monte Carlo simulations**

To develop a GEANT4 simulation representative of LCTEM conditions, a literature precedent employing GEANT4 to model an STEM was amended.<sup>34</sup> The amended Monte Carlo simulation incorporates an electron source operated at 300 keV, as is typical for an LCTEM microscope, <sup>18,24,33,35,36</sup> and the underlying physics accounts for multiple scattering under the Penelope system.<sup>37</sup> The three-dimensional sample geometry and the size of the world were set to be equal sizes so that only scattering in the sample would be considered.

The size of the sample mirrors the typical liquid cell window size of 50  $\times$  50  $\mu m$  in the x and y dimensions. We investigated z dimensions of 100, 200, and 500 nm, and 1, 2, 5, and 10  $\mu m$ . The sample was made of either DMF, methanol, or water. These solvents were programmed into the simulation by specifying their elemental composition and density. Each simulation was repeated three times with one million primary electrons. To assess electron-solvent interactions for each solvent, the number of SEs, the absorbed energy, and the absorbed dose were measured by a detector placed in the center of the sample geometry. For the three repeated simulations, the average number of SEs, absorbed energy, and absorbed dose were calculated with standard deviations.

#### **COMSOL** radiolysis modeling

To create a model for solvent radiolysis, we utilized the reaction engineering module of COMSOL with the PARADISO solver. The concentration with time (C(t)) of each radiolytic product in each solvent was measured by summing the reaction rates of individual reactions ( $R_i$ ) between radiolytic products and adding in the yield from direct irradiation ( $G_i$ ), according to the equation:

Note that  $G_r$  is measured in units of M s<sup>-1</sup> and is dependent on the G value of the given radiolytic species (G, molecules/100 eV) and the dose rate (D, Gy s<sup>-1</sup>), as shown in the equation below, where  $\rho$  is the density of the solvent (g cm s<sup>-3</sup>) and F is Faraday's constant:<sup>25</sup>

For our modeling, we used a 300 keV electron beam with a 1  $\mu$ m radius (a) and 1 nA current (I). This resulted in a dose rate of 7.7  $\times$  10<sup>7</sup> Gy s<sup>-1</sup> for methanol, 7.51  $\times$  10<sup>7</sup> Gy s<sup>-1</sup> for DMF, and 7.50  $\times$  10<sup>7</sup> Gy s<sup>-1</sup> for water. These values were calculated according to the equation below and are slightly different due to the difference in the density-normalized stopping power (S) for the three solvents. <sup>25,40</sup>

#### **SUPPLEMENTAL INFORMATION**

Supplemental information can be found online at https://doi.org/10.1016/j.xcrp. 2022.100772.

#### **ACKNOWLEDGMENTS**

Research in the N.C.G. group was conducted with government support under and awarded by the DOD through the ARO (W911NF-17-1-0326). In addition, the N.C.G. group thanks the NSF for support through a joint research grant (CHE-MSN 1905270). This research used EPIC facility of Northwestern University's NUANCE Center, which has received support from the Soft and Hybrid Nanotechnology Experimental (SHyNE) Resource (NSF ECCS-1542205), the MRSEC program

#### Article



(NSF DMR1720139) at the Materials Research Center; the International Institute for Nanotechnology (IIN), the Keck Foundation, and the State of Illinois, through the IIN. This work also made use of the IMSERC at Northwestern University, which has received support from the SHyNE Resource (NSF ECCS-1542205); the State of Illinois and International Institute for Nanotechnology (IIN). J.K. gratefully acknowledges support from the Ryan Fellowship and the IIN at Northwestern University. J.K. would like to acknowledge Small Molecule Analytical Chemistry (SMAC) at Genentech for providing the summer internship opportunity to support the simulation and modeling part of this research.

#### **AUTHOR CONTRIBUTIONS**

J.K. and N.C.G. devised the project. J.K. performed LCTEM, MALDI-IMS, and COM-SOL modeling and drafted the paper. K.G. assisted in Monte Carlo simulations. N.Z. and C.V. assisted in Monte Carlo simulations and COMSOL modeling. All authors wrote and edited the manuscript. All authors have given approval to the final version of the manuscript.

#### **DECLARATION OF INTERESTS**

The authors declare no competing interests.

Received: December 6, 2021 Revised: January 7, 2022 Accepted: January 21, 2022 Published: February 17, 2022

#### **REFERENCES**

- Holder, S.J., and Sommerdijk, N.A. (2011). New micellar morphologies from amphiphilic block copolymers: disks, toroids and bicontinuous micelles. Polym. Chem. 2, 1018–1028.
- Filice, M., Marciello, M., Morales, M.d.P., and Palomo, J.M. (2013). Synthesis of heterogeneous enzyme-metal nanoparticle biohybrids in aqueous media and their applications in C-C bond formation and tandem catalysis. Chem. Commun. 49, 6876-6878. https://doi.org/10.1039/ C3CC42475H.
- Persigehl, P., Jordan, R., and Nuyken, O. (2000). Functionalization of amphiphilic poly (2-oxazoline) block copolymers: a novel class of macroligands for micellar catalysis. Macromolecules 33, 6977–6981.
- 4. Förster, S. (2003). Amphiphilic block copolymers for templating applications. Colloid Chem. *I*, 1–28.
- Holmberg, K. (2004). Surfactant-templated nanomaterials synthesis. J. Colloid Interf. Sci. 274, 355–364. https://doi.org/10.1016/j.jcis. 2004.04.006.
- Lazzari, M., and López-Quintela, M.A. (2003). Block copolymers as a tool for nanomaterial fabrication. Adv. Mater. 15, 1583–1594.
- Wu, B.-H., Zhu, L.-W., Ou, Y., Tang, W., Wan, L.-S., and Xu, Z.-K. (2015). Systematic investigation on the formation of honeycombpatterned porous films from amphiphilic block copolymers. J. Phys. Chem. C 119, 1971–1979.

- Zhou, S., Gu, P., Wan, H., Zhu, Y., Wang, A., Shi, H., Xu, Q., and Lu, J. (2020). TPE-containing amphiphilic block copolymers: synthesis and application in the detection of nitroaromatic pollutants. Polym. Chem. 11, 7244–7252. https://doi.org/10.1039/D0PY01162B.
- Clodt, J.I., Rangou, S., Schröder, A., Buhr, K., Hahn, J., Jung, A., Filiz, V., and Abetz, V. (2013). Carbohydrates as additives for the formation of isoporous PS-b-P4VP diblock copolymer membranes. Macromol. Rapid Commun. 34, 190–194.
- Franken, L.E., Boekema, E.J., and Stuart, M.C.A. (2017). Transmission electron microscopy as a tool for the characterization of soft materials: application and interpretation. Adv. Sci. 4, 1600476. https://doi.org/10.1002/ advs.201600476.
- Henderson, R., and Unwin, P.N.T. (1975). Threedimensional model of purple membrane obtained by electron microscopy. Nature 257, 28–32.
- Dubochet, J., Adrian, M., Chang, J.-J., Homo, J.-C., Lepault, J., McDowall, A.W., and Schultz, P. (1988). Cryo-electron microscopy of vitrified specimens. Q. Rev. Biophys. 21, 129–228.
- Frank, J., Radermacher, M., Penczek, P., Zhu, J., Li, Y., Ladjadj, M., and Leith, A. (1996). SPIDER and WEB: processing and visualization of images in 3D electron microscopy and related fields. J. Struct. Biol. 116, 190–199.
- 14. Oostergetel, G., Esselink, F., and Hadziioannou, G. (1995). Cryo-electron

- microscopy of block copolymers in an organic solvent. Langmuir 11, 3721–3724.
- Wirix, M.J., Bomans, P.H., Friedrich, H., Sommerdijk, N.A., and de With, G. (2014). Three-dimensional structure of P3HT assemblies in organic solvents revealed by cryo-TEM. Nano Lett. 14, 2033–2038.
- Matatyaho Ya'akobi, A., and Talmon, Y. (2021). Extending cryo-EM to nonaqueous liquid systems. Acc. Chem. Res. 54, 2100–2109.
- Cookman, J., Hamilton, V., Price, L.S., Hall, S.R., and Bangert, U. (2020). Visualising early-stage liquid phase organic crystal growth via liquid cell electron microscopy. Nanoscale 12, 4636– 4644. https://doi.org/10.1039/C9NR08126G.
- Lyu, J., Gong, X., Lee, S.-J., Gnanasekaran, K., Zhang, X., Wasson, M.C., Wang, X., Bai, P., Guo, X., Gianneschi, N.C., and Farha, O.K. (2020). Phase transitions in metal-organic frameworks directly monitored through in situ variable temperature liquid-cell transmission electron microscopy and in situ X-ray diffraction. J. Am. Chem. Soc. 142, 4609–4615. https://doi.org/10.1021/jacs.0c00542.
- Vailonis, K.M., Gnanasekaran, K., Powers, X.B., Gianneschi, N.C., and Jenkins, D.M. (2019). Elucidating the growth of metal-organic nanotubes combining isoreticular synthesis with liquid-cell transmission electron microscopy. J. Am. Chem. Soc. 141, 10177– 10182. https://doi.org/10.1021/jacs.9b04586.
- 20. Touve, M.A., Figg, C.A., Wright, D.B., Park, C., Cantlon, J., Sumerlin, B.S., and Gianneschi, N.C. (2018). Polymerization-induced self-



## Cell Reports Physical Science Article

- assembly of micelles observed by liquid cell transmission electron microscopy. ACS Cent. Sci. 4, 543–547. https://doi.org/10.1021/acscentsci.8b00148.
- Parent, L.R., Bakalis, E., Ramírez-Hernández, A., Kammeyer, J.K., Park, C., de Pablo, J., Zerbetto, F., Patterson, J.P., and Gianneschi, N.C. (2017). Directly observing micelle fusion and growth in solution by liquid-cell transmission electron microscopy. J. Am. Chem. Soc. 139, 17140–17151. https://doi.org/ 10.1021/jacs.7b09060.
- Li, C., Tho, C.C., Galaktionova, D., Chen, X., Král, P., and Mirsaidov, U. (2019). Dynamics of amphiphilic block copolymers in an aqueous solution: direct imaging of micelle formation and nanoparticle encapsulation. Nanoscale 11, 2299–2305.
- Ianiro, A., Wu, H., van Rijt, M.M., Vena, M.P., Keizer, A.D., Esteves, A.C.C., Tuinier, R., Friedrich, H., Sommerdijk, N.A., and Patterson, J.P. (2019). Liquid-liquid phase separation during amphiphilic self-assembly. Nat. Chem. 11, 320–328.
- Korpanty, J., Parent, L.R., and Gianneschi, N.C. (2021). Enhancing and mitigating radiolytic damage to soft matter in aqueous phase liquid-cell transmission electron microscopy in the presence of gold nanoparticle sensitizers or isopropanol scavengers. Nano Lett. 21, 1141– 1149. https://doi.org/10.1021/acs.nanolett. 0c04636.
- Schneider, N.M., Norton, M.M., Mendel, B.J., Grogan, J.M., Ross, F.M., and Bau, H.H. (2014). Electron-water interactions and implications for liquid cell electron microscopy. J. Phys. Chem. C 118, 22373–22382. https://doi.org/10. 1021/in507400h
- Woehl, T.J., Jungjohann, K.L., Evans, J.E., Arslan, I., Ristenpart, W.D., and Browning, N.D. (2013). Experimental procedures to mitigate electron beam induced artifacts during in situ fluid imaging of nanomaterials. Ultramicroscopy 127, 53–63. https://doi.org/ 10.1016/j.ultramic.2012.07.018.
- Parent, L.R., Bakalis, E., Proetto, M., Li, Y., Park, C., Zerbetto, F., and Gianneschi, N.C. (2018). Tackling the challenges of dynamic experiments using liquid-cell transmission electron microscopy. Acc. Chem. Res. 51, 3–11. https://doi.org/10.1021/acs.accounts. 7b00331.
- Gibson, W., and Patterson, J.P. (2021). Liquid phase electron microscopy provides opportunities in polymer synthesis and manufacturing. Macromolecules 54, 4986– 4996.
- 29. Woehl, T.J., Moser, T., Evans, J.E., and Ross, F.M. (2020). Electron-beam-driven chemical processes during liquid phase transmission electron microscopy. MRS Bull. 45, 746–753.
- Wang, M., Leff, A.C., Li, Y., and Woehl, T.J. (2021). Visualizing ligand-mediated bimetallic nanocrystal formation pathways with in situ liquid-phase transmission electron microscopy synthesis. ACS Nano 15, 2578–2588.

- Qin, F., Wang, Z., and Wang, Z.L. (2016). Anomalous growth and coalescence dynamics of Hybrid perovskite nanoparticles observed by liquid-cell transmission electron microscopy. ACS Nano 10, 9787–9793. https:// doi.org/10.1021/acsnano.6b04234.
- Tsarfati, Y., Rosenne, S., Weissman, H., Shimon, L.J.W., Gur, D., Palmer, B.A., and Rybtchinski, B. (2018). Crystallization of organic molecules: nonclassical mechanism revealed by direct imaging. ACS Cent. Sci. 4, 1031–1036. https:// doi.org/10.1021/acscentsci.8b00289.
- Touve, M.A., Carlini, A.S., and Gianneschi, N.C. (2019). Self-assembling peptides imaged by correlated liquid cell transmission electron microscopy and MALDI-imaging mass spectrometry. Nat. Commun. 10, 4837. https:// doi.org/10.1038/s41467-019-12660-1.
- 34. Gnanasekaran, K., de With, G., and Friedrich, H. (2018). Quantification and optimization of ADF-STEM image contrast for beam-sensitive materials. R. Soc. Open Sci. 5, 171838.
- Gnanasekaran, K., Chang, H., Smeets, P.J.M., Korpanty, J., Geiger, F.M., and Gianneschi, N.C. (2020). In situ Ni2+ stain for liposome imaging by liquid-cell transmission electron microscopy. Nano Lett. 20, 4292–4297. https:// doi.org/10.1021/acs.nanolett.0c00898.
- Gnanasekaran, K., Vailonis, K.M., Jenkins, D.M., and Gianneschi, N.C. (2020). In situ monitoring of the seeding and growth of silver metal– organic nanotubes by liquid-cell transmission electron microscopy. ACS Nano 14, 8735–8743.
- Amako, K., Guatelli, S., Ivanchencko, V., Maire, M., Mascialino, B., Murakami, K., Pandola, L., Parlati, S., Pia, M., and Piergentili, M. (2006). Geant4 and its validation. Nucl. Phys. B Proc. Suppl. 150, 44–49.
- Williams, D.B., and Carter, C.B. (2009). Transmission Electron Microscopy: A Textbook for Materials Science (Springer).
- Ross, F.M. (2015). Opportunities and challenges in liquid cell electron microscopy. Science 350, aaa9886. https://doi.org/10.1126/ science.aaa9886.
- Berger, M.J., Coursey, J.S., Zucker, M.A., and Chang, J. (2017). NIST standard reference database. https://physics.nist.gov/ PhysRefData/Star/Text/ESTAR.html.
- Woehl, T.J., and Abellan, P. (2017). Defining the radiation chemistry during liquid cell electron microscopy to enable visualization of nanomaterial growth and degradation dynamics. J. Microsc. 265, 135–147. https://doi. org/10.1111/jmi.12508.
- 42. Forrester, A.R., Hay, J.M., and Thomson, R.H. (1968). Organic Chemistry of Stable Free Radicals (Academic Press).
- Henry, D.J., Parkinson, C.J., Mayer, P.M., and Radom, L. (2001). Bond dissociation energies and radical stabilization energies associated with substituted methyl radicals. J. Phys. Chem. A 105, 6750–6756. https://doi.org/10.1021/ jp010442c.

- Chatgilialoglu, C., Crich, D., Komatsu, M., and Ryu, I. (1999). Chemistry of acyl radicals. Chem. Rev. 99, 1991–2070. https://doi.org/10.1021/ cr9601425.
- Overend, R., and Paraskevopoulos, G. (1978). Rates of hydroxyl radical reactions. 4. Reactions with methanol, ethanol, 1-propanol, and 2propanol at 296 K. J. Phys. Chem. 82, 1329–1333.
- Janik, I., Ulanski, P., Hildenbrand, K., Rosiak, J.M., and von Sonntag, C. (2000). Hydroxylradical-induced reactions of poly(vinyl methyl ether): a pulse radiolysis, EPR and product study in deoxygenated and oxygenated aqueous solutions. J. Chem. Soc. Perkin Trans. 2, 2041–2048. https://doi.org/10.1039/ B004777P.
- Kozicki, M., Kujawa, P., and Rosiak, J.M. (2002). Pulse radiolysis study of diacrylate macromonomer in aqueous solution. Radiat. Phys. Chem. 65, 133–139. https://doi.org/10. 1016/S0969-806X(02)00209-8.
- Ulanski, P., Bothe, E., Hildenbrand, K., Rosiak, J.M., and von Sonntag, C. (1996). Hydroxylradical-induced reactions of poly(acrylic acid); a pulse radiolysis, EPR and product study. Part I. Deoxygenated aqueous solutions. J. Chem. Soc. Perkin Trans. 2, 13–22. https://doi.org/10. 1039/P29960000013.
- von Sonntag, C. (2003). Free-radical-induced chain scission and cross-linking of polymers in aqueous solution—an overview. Radiat. Phys. Chem. 67, 353–359. https://doi.org/10.1016/ S0969-806X(03)00066-5.
- van Zoelen, W., Asumaa, T., Ruokolainen, J., Ikkala, O., and Ten Brinke, G. (2008). Phase behavior of solvent vapor annealed thin films of PS-b-P4VP (PDP) supramolecules. Macromolecules 41, 3199–3208.
- O'Driscoll, S., Demirel, G., Farrell, R.A., Fitzgerald, T.G., O'Mahony, C., Holmes, J.D., and Morris, M.A. (2011). The morphology and structure of PS-b-P4VP block copolymer films by solvent annealing: effect of the solvent parameter. Polym. Adv. Tech. 22, 915–923.
- Gowd, E.B., Koga, T., Endoh, M.K., Kumar, K., and Stamm, M. (2014). Pathways of cylindrical orientations in PS-b-P4VP diblock copolymer thin films upon solvent vapor annealing. Soft Matter 10, 7753–7761.
- 53. Korpanty, J., Parent, L.R., Hampu, N., Weigand, S., and Gianneschi, N.C. (2021). Thermoresponsive polymer assemblies via variable temperature liquid-phase transmission electron microscopy and small angle X-ray scattering. Nat. Commun. 12, 6568. https://doi.org/10.1038/s41467-021-26773-z.
- Kumar, L., Horechyy, A., Bittrich, E., Nandan, B., Uhlmann, P., and Fery, A. (2019). Amphiphilic block copolymer micelles in selective solvents: the effect of solvent selectivity on micelle formation. Polymers 11, 1882.
- Ye, X., Niroomand, H., Hu, S., and Khomami, B. (2015). Block copolymer micelle formation in a solvent good for all the blocks. Colloid Polym. Sci. 293, 2799–2805.